

Second law and thermal analyses of non-Newtonian nanofluid double-diffusive natural convection within a two-hot-baffles-equipped C-shaped domain impacted by magnetic field

Second law
and thermal
analyses

581

Received 24 February 2023
Revised 19 July 2023
14 September 2023
21 September 2023
Accepted 30 September 2023

Kashif Irshad

Interdisciplinary Research Center for Renewable Energy and Power Systems (IRC-REPS), King Fahd University of Petroleum and Minerals, Dhahran, Saudi Arabia

Amjad Ali Pasha

Aerospace Engineering Department, King Abdulaziz University, Jeddah, Saudi Arabia

Mohammed K. Al Mesfer and Mohd Danish

Chemical Engineering Department, College of Engineering, King Khalid University, Abha, Saudi Arabia

Manoj Kumar Nayak

Department of Mechanical Engineering, FET, ITER, Siksha 'O' Anusandhan Deemed to be University, Bhubaneswar, India

Ali Chamkha

Mechanical Engineering Department, Prince Mohammad Bin Fahd University, Al Khobar, Saudi Arabia, and

Ahmed M. Galal

Prince Sattam bin Abdulaziz University, Al Kharj, Saudi Arabia

Abstract

Purpose – The entropy and thermal behavior analyses of non-Newtonian nanofluid double-diffusive natural convection inside complex domains may captivate a bunch of scholars' attention because of the potential utilizations that they possess in modern industries, for example, heat exchangers, solar energy collectors and cooling of electronic apparatuses. This study aims to investigate the second law and thermal behavior of non-Newtonian double-diffusive natural convection (DDNC) of $Al_2O_3-H_2O$ nanofluid within a C-shaped cavity emplacing two hot baffles and impacted by a magnetic field.

The authors acknowledge the financial assistance from the Deanship of Scientific Research for grant (G. R. P./207/43), King Khalid University, Abha, KSA.

Since submission of this article, the following author has updated their affiliation: Ahmed M. Galal is at the Production Engineering and Mechanical Design Department, Faculty of Engineering, Mansoura University, Mansoura, Egypt.



Design/methodology/approach – For the governing equations of the complicated and practical system with all considered parameters to be solved via a formidable numerical approach, the finite element method acts as an approach to achieving the desired solution. This method allows us to gain a detailed solution to the studied geometry.

Findings – This investigation has been executed for the considered parameters of range, such as power-law index, baffle length, Lewis number, buoyancy ratio, Hartmann number and Rayleigh number. The main results reveal that isothermal and concentration lines are significantly more distorted, indicating intensified concentration and temperature distributions because of the growth of baffle length (L). Nu_{ave} decreases by 8.4% and 0.8% while it enhances by 49.86% and 33.87%, respectively, because of growth in the L from 0.1 to 0.2 and 0.2 to 0.3.

Originality/value – Such a comprehensive study on the second law and thermal behavior of DDNC of $Al_2O_3-H_2O$ nanofluid within a C-shaped cavity emplacing two hot baffles and impacted by magnetic field has not yet been carried out.

Keywords Double-diffusive natural convection, C-shaped cavity, Hot baffles, Magnetic field, Non-Newtonian nanofluid, Entropy generation

Paper type Research paper

Nomenclature

(x, y) = Cartesian coordinates;
 (u, v) = velocity components;
 (U, V) = non-dimensional velocities;
 τ = shear stress tensor;
 T = temperature;
 C = solutal concentration;
 D = mass diffusivity;
 p = pressure;
 P = non-dimensional pressure;
 g = acceleration due to gravity;
 θ = non-dimensional temperature;
 ϕ = volume fraction;
 Nu = Nusselt number;
 En_T = entropy generation number;
 Be = Bejan number;
 ρ = density;
 μ_{nf} = consistency index;
 Γ_{nf} = apparent viscosity;
 N = power-law index;
 (ρC_p) = specific heat capacity;
 β_T = thermal expansion coefficient;
 β_C = solutal expansion coefficient;
 K = thermal conductivity;
 σ = electrical conductivity;
 Pr = Prandtl number;
 Ha = Hartman number;
 Ra = Rayleigh number;
 Le = Lewis number;
 Π_b = apparent viscosity; and
 N = buoyancy ratio.

Subscripts

ave = average;
loc = local;
c = cold;
f = base fluid; and
s = solid particle.

1. Introduction

Nanotechnology has emerged as one of the most fabulous fields of study to be required in many scientific fields and the industrial world because of its capacity to make and use materials with particle sizes of around 1–100 nm. The emphasis on nanofluids in this discipline is because of the quick growth of nanotechnology and the expanding success of its diverse applications. In essence, the production of nanofluids involves the dispersion of one or more types of solid particles (such as Zn, Ti, Al, Fe, ZnO, TiO₂, Al₂O₃, Fe₃O₄, SWCNT and MWCNT) with a diameter smaller than 100 nm in a base fluid (such as motor oil, ethylene glycol and water) (Choi and Eastman, 1995; Awais *et al.*, 2020). Thermal extrusion systems, solar thermal systems, heat exchangers, microelectronic cooling, the automobile sector, air conditioning, ventilation and medicine are examples of multidisciplinary uses of nanofluids. Hydrothermal exploration of a solar collector loaded with nanofluid considering the Koo–Kleinstreuer–Li approach was done by Shariatifard *et al.* (2022). The thermal performance of a sola collector considering the impact of nanofluid was explored by Menbari *et al.* (2016). The second law examination of magnetized free convection inside a porous–wavy–hexagonal container was performed by Seyyedi *et al.* (2020), and Aly and Alsedais (2023) numerically examined the buoyancy-driven flow of a new type of nanofluid inside a porous H-shaped chamber. Verma *et al.* (2017) performed an experimental study on the nanofluid-based solar collector. Thermodynamic assessment of a solar collector working with a hybrid nanofluid was analyzed by Okonkwo *et al.* (2020), and Roy and Monira (2023) explored the magnetized free convection within a nanofluid-filled open porous wavy container. The influence of diverse heater shapes on the thermal performance of hybrid nanofluid inside a novel domain was examined by Biswas *et al.* (2023). Naseer *et al.* (Hamza *et al.*, 2023) analyzed the growth of heat transfer inside a hybrid NF-loaded corrugated domain with a heated plane inside. Mahian *et al.* (2019) emphasized the fundamental physical characteristics and three-dimensional research while highlighting some advancements in nanofluid flow modeling across various flow regimes. The flow of nanofluids in mini-, micro- and cavities under various physical conditions and boundary conditions was explored by Huminic and Huminic (2020). Dogonchi *et al.* (2020) conducted a simulation of the hydrothermal characteristics of Cu–H₂O nanofluid-free convection inside a porous annulus while taking several heater settings into consideration. In their study, it was found that the heat transfer rate was enhanced because of the amplification of the Rayleigh and Darcy numbers. Further, augmentation of the Rayleigh number increases the nanofluid velocity.

The term “double-diffusive convection,” often referred to as “thermosolutal convection,” refers to fluid flows caused by buoyant effects brought on by concentration and temperature gradients that are applied and have separate rates of diffusion. Mass transfer also occurs when there is heat transfer in practice, as seen in many industrial domains. One of these areas is crystal growth, where it has been discovered that fluid phase transport phenomena have a significant impact on the crystal’s structure and quality. DDNC heat transfer is a very important phenomenon in diversified engineering and industrial applications, including high-performing insulation in buildings, injection molding, grain storing, glass

manufacturing, microchannels, air-conditioners, electronic devices' cooling, power plants, solar collectors, etc. DDNC is also relevant in sedimentation in salt water, thermo-haline effects in horizontal convection and double-diffusion systems in oceanography. It is difficult to directly examine fluid stability, convection occurrence and transition because of its complexity in practical situations (Turner, 1974). The physical model of the DDNC system that conveys its intricate operation is of particular importance to researchers. Ghernoug *et al.* (2016) performed a numerical simulation on the DDNC inside a horizontal tubal ring. Magnetized DDNC in a nanofluid-loaded container with a fluctuating pipe was analyzed by M. Aly (2020). Raizah and M. Aly (2020) scrutinized the magnetic DDNC of a nanostream inside a chamber, including open pipes. They reported that increasing the length of the straight pipe can cause the heat and mass rate to grow. Rashad *et al.* (2014) explored the influence of thermal radiation and chemical reactions on the transient DDNC inside a porous container. They concluded that thermal radiation can improve the heat transfer rate. Aly and ASAI (2016) analyzed the efficacy of cross-diffusion on the DDNC inside an anisotropic chamber. The DDNC in a rectangular cavity with steady and unstable solutions was investigated by Yang and Zhao (2021). Hybrid nanofluids may be commonly applied to improve thermal characteristics in a stationary DDNC issue. Álvarez *et al.* (2022) used a vector advection–diffusion equation in conjunction with a Navier–Stokes/Brinkman type system to describe the velocity and pressure. Teamah and El-Maghlany (2010) investigated DDNC inside a lid-driven area with the composed buoyancy effects. Both lower and upper surfaces may be impermeable and insulated. Fixed diverse concentrations and temperatures may be imposed along vertical surfaces. The numerical results reveal the efficacy of Richardson and Lewis numbers and buoyancy ratio on the streamlines, concentration and temperature.

Diversified industries deal with the NC of power-law fluids (non-Newtonian fluids) in domains such as food preservation, polymer industry, cooling systems and metal processing. Recently, the NC of non-Newtonian fluids has been extensively explored with diverse solution methods by numerous researchers. In a square domain with vertical side walls that were differentially heated and exposed to constant wall temperatures, Kim *et al.* (2003) investigated the transient NC of non-Newtonian power-law liquids. For a given range of Rayleigh and Prandtl number values, they showed that the mean Nusselt number Nu rises with a lessening power-law index. Inside a non-Newtonian liquid-filled chamber, Lamsaadi *et al.* (2006) conducted a study of NC. They discovered that, in contrast to the Newtonian situation, shear-thickening behavior may have an opposite effect on the heat transfer rate. In a square domain loaded with a non-Newtonian power-law liquid and simulating it using the Finite Difference Lattice Boltzmann Method, Kefayati (2015) examined DDNC. The Rayleigh number (Ra), power-law index ($n = 0.6–1.4$), Dufour parameter ($= 0–1$), buoyancy ratio ($N = -1, 0.1, 1$) and Lewis number ($Le = 2.5, 5$) have all been studied for certain relevant parameters. With an increase in Ra , heat and mass transmission are improved. With a rise in the n for positive buoyancy ratios, heat and mass transmissions decrease. At a buoyancy ratio of $N = 1$, the power-law index has the greatest impact on the transmission of heat and mass. Mass transport is improved, and heat transfer is only marginally affected as the Lewis number rises. However, it causes heat transfer to increase for $N = -1$ and decrease for positive buoyancy ratios.

Double-diffusive natural convection appears in oceanography (Schmitt, 1994), transport of contamination across the air and crystal progress (Huppert and Sparks, 1984). Simulation of DDNC and entropy of power-law fluids inside an inclined porous zone was studied by Kefayati (2016a, 2016b, 2016c). Alomari *et al.* (2022) investigated double-diffusive mixed convection inside a split lid-driven curvilinear domain. Further, double diffusive buoyancy-

induced convection in stepwise open porous cavities filled with nanofluid was analyzed by [Hussain et al. \(2020\)](#). Magneto hydrodynamics (MHDs) may have a substantial effect on fluid flow behavior and HT enhancement. Because of this, this topic has drawn a lot of scholars who are interested in learning how this phenomenon works. MHD forces, which result from the interaction of induced electric currents and the applied magnetic field, frequently affect the flow of an electrically conducting fluid in a magnetic field. A common tool used in the production of metals that behave like non-Newtonian power-law fluids is an external magnetic field. Investigations have been made into how the magnetic field affects the double-diffusive convection process in various cavities that are susceptible to a variety of fluids and boundary conditions. For instance, [Aly et al. \(2021\)](#) explored solutal-thermo convection inside a finned domain, including a circle rectangle form, by adopting the incompressible smoothed particle hydrodynamics approach. The copper/water nanofluids are positioned within the cavity using fins. The four fins are kept at T_c and C_c and are placed in the heart of the domain sidewalls. The inner form contains a high concentration of C_h and a hot temperature of T_h . The key results demonstrate that the presence of fins is a powerful tool for cooling an NF within a finned domain. The convective flow characteristics and the motions of the nanofluid are profoundly affected by the rotation of an implanted rectangle form. Below are the modifications of the Dufour and Soret numbers; the mean Sherwood number exhibits non-monotonic activities. The magnetic power increases with increasing Hartmann number Ha , which reduces isoconcentration and isothermal distributions and inhibits the flow of nanofluids. The maximum streamlines $|\psi_{\max}|_{\max}$ is petered out by 83.32%, 80.14% and 78.06% as Ha increases from 0 to 50 at $\gamma = 0^\circ, 60^\circ$ and 90° correspondingly. The growing angle of magnetic inclination γ from 0° to 90° ameliorates $|\psi_{\max}|$ by 31.53% and 9.59% at $Ha = 50$ and 20 correspondingly. Heat and mass transfer rates may be lessened by growing Ha . [Al-Farhany et al. \(2023\)](#) studied magnetized double-diffusive mixed convection inside a curvilinear nanofluid-loaded zone with conducting fins inside. As a result of growing Reynolds number, nanoparticle volume concentration and fin length, the Nu_{ave} and Sh_{ave} rise while decreasing with raising Hartmann number. When Richardson number Ri is low, Nu_{avg} rises along with the inclination of the magnetic field, but for high Ri , the inclination angle has the opposite effect. On the other hand, for all Ri values, the Sh_{ave} rises as the magnetic field inclination does.

In fact, entropy generation indicates the energy losses in thermal systems. Therefore, precise calculation of entropy generation ensures the optimal design of the heat transfer process in diversified industries. Keeping this concept in mind, entropy generation is studied in the double diffusion natural convection of nanofluids accommodated in several cavities. [Kefayati \(2016a, 2016b, 2016c\)](#) examined the non-Newtonian power-law fluid DDNC in an open domain with a horizontal magnetic field. He discovered that for certain power-law indexes, an increment in the Ha may cause a decrease in heat and mass transmission. Heat and mass transmission lessen with the increase of the n in diverse Ra for varied Ha as the Soret and Dufour numbers equal zero. For various power-law indices and Ra , the mass transfer improves as the Soret parameter rises, whereas the heat transfer increases as the Dufour parameter rises. The behavior of heat and mass transmission is changed in opposition to a change in the power-law index by increasing the Soret and Dufour parameters. [Kefayati \(2016a, 2016b, 2016c\)](#) examined the entropy production associated with DDNC of non-Newtonian liquids in an oblique porous domain. The simulation and analysis of the entropy generation have been done for the relevant parameters such as Ra , Da , n , Le , inclined angles, Dufour and Soret parameters and buoyancy ratio. His research shows that increasing the thermal Ra increases various entropy generations while decreasing the mean Bejan number Be . The average Be sharply declines as the Da rises, causing a variety of

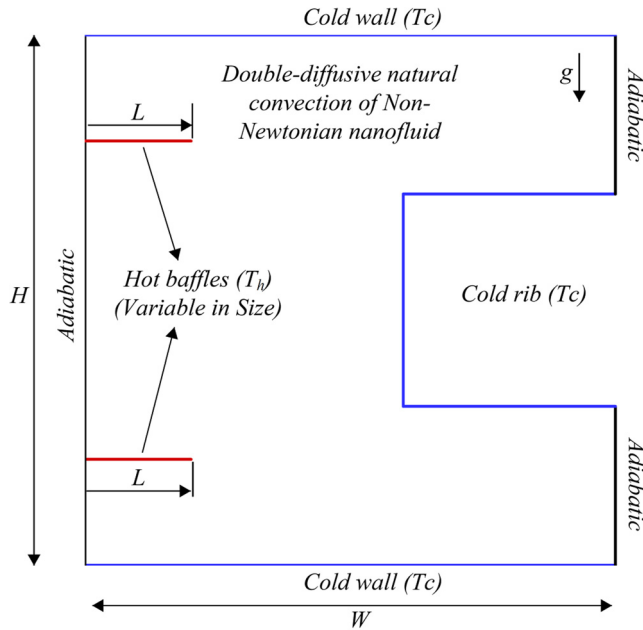
irreversibilities to grow. The mean Be decreases, and various total entropy generators are enhanced by increasing the inclination angle. The total entropy generation decreases as the inclined angle increases, and the mean Be rises as a result. The increase in Soret and Dufour parameters accelerates the formation of entropy brought on by heat conduction and fluid friction. Various entropy generations are altered by changes in the power-law index. Reddy *et al.* (2022a) studied the entropy and thermal features of a magnetized nanofluid-loaded domain. They reported that augmenting the radiation parameter as well as the volume fraction of nanofluid can improve the heat transmission rate.

The antecedent literature may well present that there may be no research linked to the magnetic implications on a system under the existence of double-diffusive natural convection and second law analysis. The study of simultaneous heat and mass transfer inside a novel geometry such as a C-shaped cavity is still challenging. The present study can be used to regulate the thermo-solutal convection and entropy under the impact of a magnetic field subjected to a C-shaped enclosure filled with non-Newtonian water nanofluid in building insulation, storing grains, microchannels, air-conditioners, cooling of electronic devices, power plants, solar collectors, etc. Entropy generation calculation ensures the better design of the heat transfer processes and the associated thermal devices in the above-mentioned fields. These challenges and usefulness motivated us to study the second law and thermal behavior of non-Newtonian double-diffusive natural convection (DDNC) of Al_2O_3 - H_2O nanofluid within a C-shaped cavity emplacing two hot baffles and impacted by a magnetic field. The finite element method (FEM) method is used in the simulation of thermo-solutal convection and entropy analysis in a hot baffled C-shaped cavity occupied by a nanofluid. The main goal of this research is to simulate and analyze the second law and DDNC of non-Newtonian flow of power-law NF in a baffled cavity by FEM under the influence of the magnetic field. The findings of FEM may be validated with foregone numerical investigations, and the efficacy of sundry and significant parameters (power-law index, Lewis number, baffle length, buoyancy ratio number and Rayleigh number) on the flow, energy and concentration fields, apparent viscosity, entropy generation number, Bejan number, local and average Nu and Sh is examined. The novelties of the present study are as follows:

- thermal behavior of non-Newtonian DDNC of Al_2O_3 - H_2O nanofluid within a C-shaped cavity emplacing two hot baffles; and
- second law analysis of non-Newtonian DDNC of Al_2O_3 - H_2O nanofluid within a C-shaped cavity subject to a magnetic field.

2. Governing equations

The geometry of the present problem is manifested in [Figure 1](#). Two hot baffles, each of length L , are emplaced on the left wall of the C-shaped cavity. These baffles may be variable in size. The vertical left and right side walls are assumed to be well insulated. The bottom and top walls remain cold. The cold rib faces the hot baffles. The flow is presumed to be steady, laminar and incompressible. The cavity is filled with non-Newtonian power-law Al_2O_3 - H_2O nanofluid. Double-diffusive natural convection accounts for the movement of nanofluid. It is assumed that a uniform magnetic field of strength B_0 is applied horizontally to the cavity. Apart from the external magnetic field, it is presumed that the induced magnetic field is insignificant. Additionally, it is believed that the imposed and induced electrical fields are insignificant. The conventional Boussinesq model for temperature and concentration comes close to describing the density change. Additionally, it is believed that the effects of radiation, chemical reactions and viscous dissipation are minimal. The



Source: Authors' work

Figure 1.
Examined geometry

regulatory equations with the Boussinesq outlook can be established as follows (Kefayati, 2016a, 2016b, 2016c; Kefayati, 2016a, 2016b, 2016c; Reddy *et al.*, 2022a; Reddy *et al.*, 2022b):

$$\partial_y v + \partial_x u = 0 \quad (1)$$

$$\rho_{nf}(v\partial_y u + u\partial_x u) = -\partial_x p + (\partial_x \tau_{xx} + \partial_y \tau_{yx}) \quad (2)$$

$$\begin{aligned} \rho_{nf}(v\partial_y v + u\partial_x v) = & -\partial_y p + (\partial_x \tau_{xy} + \partial_y \tau_{yy}) + \rho_{nf} \beta_{nf} g(T - T_c) + \rho_{nf} \beta_{c,nf} g(c - c_c) \\ & - \sigma_{nf} B_0^2 v \end{aligned} \quad (3)$$

$$(\rho C_p)_{nf}(v\partial_y T + u\partial_x T) = k_{nf}(\partial_{yy} T + \partial_{xx} T) \quad (4)$$

$$(u\partial_x c + v\partial_y c) = D(\partial_{xx} c + \partial_{yy} c) \quad (5)$$

Here, (u, v) may be x–y parts of velocity, ρ_{nf} , μ_{nf} , k_{nf} , $(\rho C_p)_{nf}$, $\beta_{T,nf}$, $\beta_{C,nf}$ and p are density, dynamic viscosity, thermal conductivity, specific heat capacity, thermal expansion coefficient, solutal expansion coefficient and pressure of nanofluid, respectively; g is acceleration because of gravity; T and C are temperature and solutal concentration within the cavity, respectively; T_c and C_c are temperature and solutal concentration of cold walls and cold rib, respectively; D is the mass diffusivity; and τ be taken as shear stress tensor.

The τ can be characterized using the power-law (Ostwald-de Waele) viewpoint (Hussain et al., 2020; Aly et al., 2021):

$$\begin{aligned} \tau_{ij} &= \Gamma_{nf} \left(\frac{\partial u_i}{\partial x_j} + \frac{\partial u_j}{\partial x_i} \right) \\ \Gamma_{nf} &= \mu_{nf} \left[2(\partial_x u)^2 + 2(\partial_y v)^2 + (\partial_y u + \partial_x v)^2 \right]^{\frac{n-1}{2}} \end{aligned} \tag{6}$$

Here μ_{nf} , Γ_{nf} and n represent the consistency index, the apparent viscosity and the power-law index, respectively. The effective dynamic viscosity, specific heat capacity, thermal conductivity, thermal expansion coefficient, electrical conductivity and density of Al_2O_3 - H_2O nanofluid may well be represented as (Model I):

$$\begin{aligned} \mu_{nf} &= (1 + 4.93\phi + 222.4\phi^2)\mu_f, \quad (\rho C_p)_{nf} = (1 - \phi)(\rho C_p)_f + \phi(\rho C_p)_s \\ k_{nf} &= (1 + 2.944\phi + 19.672\phi^2)k_f, \quad (\rho\beta)_{nf} = (1 - \phi)(\rho\beta)_f + \phi(\rho\beta)_s \\ \sigma_{nf} &= \left[1 + \frac{3\phi((\sigma_s/\sigma_f) - 1)}{((\sigma_s/\sigma_f) + 2) - \phi(\sigma_s/\sigma_f) - 1} \right] \sigma_f, \quad \rho_{nf} = (1 - \phi)\rho_f + \phi\rho_s \end{aligned} \tag{7}$$

where ϕ is the volume fraction, k_f is the thermal conductivity of the base fluid, μ_f is the dynamic viscosity of the base fluid, $(\rho C_p)_f$, $(\rho C_p)_s$ are specific heat capacity of base fluid, Al_2O_3 nanoparticle, β_f , β_s are the thermal expansion coefficient of base fluid, Al_2O_3 nanoparticle, σ_{nf} , σ_f , σ_s are respectively the electrical conductivity of nanofluid, base fluid and Al_2O_3 nanoparticle, ρ_{nf} , ρ_f , ρ_s are respectively the density of nanofluid, base fluid and Al_2O_3 nanoparticle. Table 1 portrays the thermo-physical specifications of Al_2O_3 and H_2O .

Considering the following parameters:

$$\theta = \frac{T - T_c}{\Delta T}, \quad P = \frac{pW^2}{\rho_f \alpha_f^2}, \quad (V, U) = \frac{(v, u)W}{\alpha_f}, \quad (Y, X) = \frac{(y, x)}{W} \tag{8}$$

Here, L is the length of the baffle.

Equations (1)–(5) and the boundary conditions in their non-dimensional forms can be determined as:

$$(V\partial_Y U + U\partial_X U) = -\partial_X P + \left[\frac{(1 + 4.93\phi + 222.4\phi^2)}{\rho_{nf}/\rho_f} \right] \text{Pr} \left[\begin{aligned} &\partial_X (2\Pi_{nf}\partial_X U) \\ &+ \partial_Y (\Pi_{nf}(\partial_X V + \partial_Y U)) \end{aligned} \right] \tag{9}$$

$$\begin{aligned} (V\partial_Y V + U\partial_X V) &= -\partial_Y P + \left[\frac{(1 + 4.93\phi + 222.4\phi^2)}{\rho_{nf}/\rho_f} \right] \text{Pr} \left[\begin{aligned} &\partial_Y (2\Pi_{nf}\partial_X U) \\ &+ \partial_X (\Pi_{nf}(\partial_X V + \partial_Y U)) \end{aligned} \right] \\ &+ \left[\frac{(\rho\beta)_{nf}}{\rho_{nf}\beta_f} \right] Ra\text{Pr}(\theta + NC) - \left[\frac{\sigma_{nf}/\sigma_f}{\rho_{nf}/\rho_f} \right] Ha^2\text{Pr}V \end{aligned} \tag{10}$$

$$(V\partial_Y\theta + U\partial_X\theta) = \left[\frac{(1 + 2.944\phi + 19.672\phi^2)}{(\rho C_p)_{nf}/(\rho C_p)_f} \right] (\partial_{YY}\theta + \partial_{XX}\theta) \quad (11)$$

$$Le(U\partial_X C + V\partial_Y C) = \partial_{XX}C + \partial_{YY}C \quad (12)$$

$$\Pi_b = \left[2(\partial_X U)^2 + 2(\partial_Y V)^2 + (\partial_Y U + \partial_X V)^2 \right]^{\frac{n-1}{2}} \quad (13)$$

The boundary conditions are (Mahmoodi and Hashemi, 2012):

$$\begin{aligned} U = 0, \partial_X\theta = 0, V = 0 & \quad \text{on right and left surfaces} \\ \theta = 0, C = 0, V = U = 0 & \quad \text{on bottom and top surfaces and on the right rib} \\ \theta = 1, C = 0, V = U = 0 & \quad \text{on baffles} \end{aligned} \quad (14)$$

Here Le , Ha , Π_b , Pr , Ra , N and n are the Lewis number (ratio of thermal diffusivity to mass diffusivity) and Hartmann number (ratio of electromagnetic force to viscous force), non-dimensional apparent viscosity, Prandtl number (ratio of kinematic viscosity to thermal diffusivity) and Rayleigh number (product of Grashof number and Prandtl number), buoyancy ratio and power-law index, respectively. The Nusselt (Nu) and Sherwood numbers (Sh), entropy generation (En) and Bejan number (Be), on the other hand, can be characterized as:

$$Nu_{loc.} = (1 + 2.944\phi + 19.672\phi^2)\partial_r\theta|_{on\ the\ right\ rib}, Nu_{ave.} = \frac{1}{S}\int_0^S Nu_{loc.} ds \quad (15)$$

$$Sh_{loc.} = \partial_r C, Sh_{ave.} = \frac{1}{S}\int_0^S Sh_{loc.} ds \quad (16)$$

$$\begin{aligned} EG_{local} = & \left[(1 + 4.93\phi + 222.4\phi^2) \right] \Pi_{nf} \Delta_1 \left[2(\partial_Y V)^2 + 2(\partial_X U)^2 + (\partial_X V + \partial_Y U)^2 \right] \\ & + \frac{\sigma_{nf}}{\sigma_f} \Delta_1 (HaV)^2 + \left[(1 + 2.944\phi + 19.672\phi^2) \right] \left[(\partial_Y\theta)^2 + (\partial_X\theta)^2 \right] \\ & + \Delta_2 \left[(\partial_Y C)^2 + (\partial_X C)^2 \right] + \Delta_3 \left[(\partial_Y C)(\partial_Y\theta) + (\partial_X C)(\partial_X\theta) \right] \end{aligned} \quad (17)$$

$$En_{Total} = \int_V En_{Local} dV. \quad (18)$$

$$Be_{loc} = \frac{\text{Entropy owing to heat transfer}}{En_{Local}}, Be_{ave} = \frac{\int_A Be_{loc} dA}{\int_A dA} \quad (19)$$

here, the Δ_1 , Δ_2 and Δ_3 's values are 10^{-4} , 0.5 and 10^{-2} , respectively, and S is the cold rib's length and r may be the vector normal to it.

3. Numerical approach and validation

This research applies FEM to solve the governing equations of non-Newtonian DDNC of $Al_2O_3-H_2O$ NF within a C-shaped domain with two hot baffles located in the right wall and impacted by a magnetic field. In the FEM, the strategy is that numerous small-scale triangular-shaped elements may be created inside the domain, and then for each of them, residual equations through the Galerkin method would be constructed. In the next step, these equations must be solved via the Newton–Raphson technique. The readers can refer to the references (Usman *et al.*, 2019; Basak *et al.*, 2006) for further information. The grid independence study of the current problem, on the other hand, is shown in Table 1, which indicates that 15,365 elements are suitable for further simulations. The current findings’ reliability may well be checked by comparing them with Kahveci’s results (Kahveci, 2010) as depicted in Figure 2 (a) and with Raisi’s outcomes (Raisi, 2016) for the NC of a non-Newtonian fluid inside a container as presented in Figure 2(b). These figures illustrate a superb concurrence between the outcomes.

4. Results and discussion

In this portion, the CFD results of non-Newtonian DDNC of $Al_2O_3-H_2O$ NF inside a C-shaped domain having two hot baffles of variable size are examined. The cavity has been exposed to the applied magnetic field. The physical problem is converted to a mathematical form that consists of a set of nonlinear partial differential equations, namely, continuity, momentum and energy equations. The numerical simulation using FEM has been carried out over the governing equations for the emerging physical parameters. In this discussion, the efficacy of power-law index ($n = 0.8, 1.2, 1.5, 1.8$), baffle length ($L = 0.1, 0.2, 0.3$), Lewis number ($Le = 1, 5, 9$), buoyancy ratio ($N = 1, 3, 5$), Hartmann number ($Ha = 0, 40$) and Rayleigh number ($Ra = 10^5, 10^6$) on streamlines (ψ), velocities (U and V), isotherms (θ), isoconcentration (C), apparent viscosity (Π), local and average Bejan number (Be_{loc}, Be_{ave}) and entropy generation (En_T) at a fixed volume fraction ($\phi = 2\%$) has been revealed.

4.1 Influence of n

Figure 3 introduces the variability of streamlines, velocities, θ , concentrations, Be_{loc} , Be_{ave} and entropy generation with n at $Le = 5$, $Ha = 0$, $N = 1$, $Ra = 10^6$ and $\phi = 2\%$. Streamlines are distributed symmetrically in the entire enclosure, starting from the region between two hot baffles and ending at the regions inside the upper and lower arms of the enclosure, irrespective of the value of n . At $n = 1.2$, circulation zones rotate in clockwise directions. A growth in n may cause a contraction of streamlines. Actually, a rise in n weakens the convection process. It may be caused by the buoyancy force’s weakness in dilatant flow. This means that heated fluid with a low density near hot baffles moves toward the cold ribs because of strong buoyancy. However, increasing n to 1.2, 1.5 and 1.8 may yield a light distortion in the streamlines neighboring cold walls (lower and upper) and cold ribs. The ($|\psi_{min}|$) drops from 37.0453 to 16.3298 when n increases from 0.8 to 1.2, while it further drops from 7.60408 to 3.77294 with a rise in n from 1.5 to 1.8. The $|\psi_{max}|$ whittles down from 1.20192 to 0.485747 when n increases from 1.2 to 1.5, while it peters out from 0.485747 to

Table 1.
Grid independence study

Elements	1,967	5,821	10,594	15,365	18,753
Sh _{ave} .	2.1487	2.6832	2.9781	3.0758	3.0799
Source: Authors’ work					

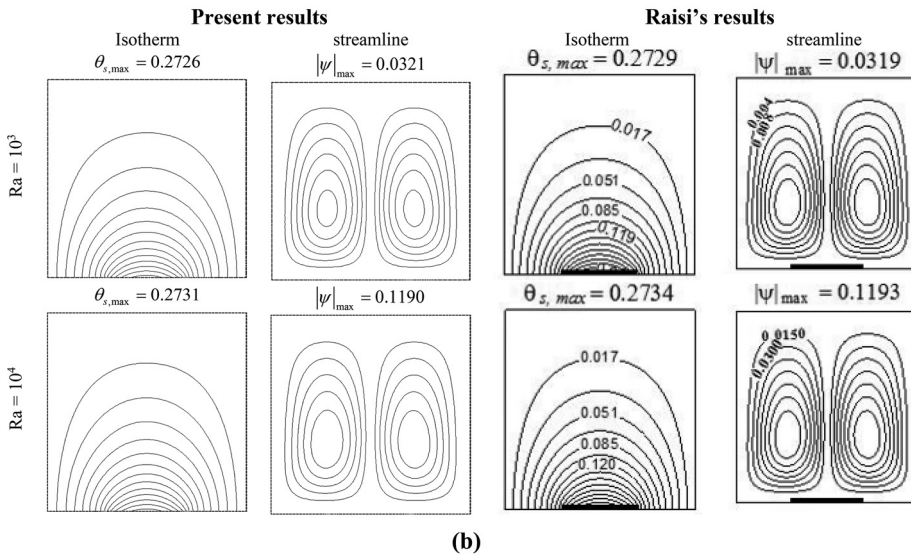
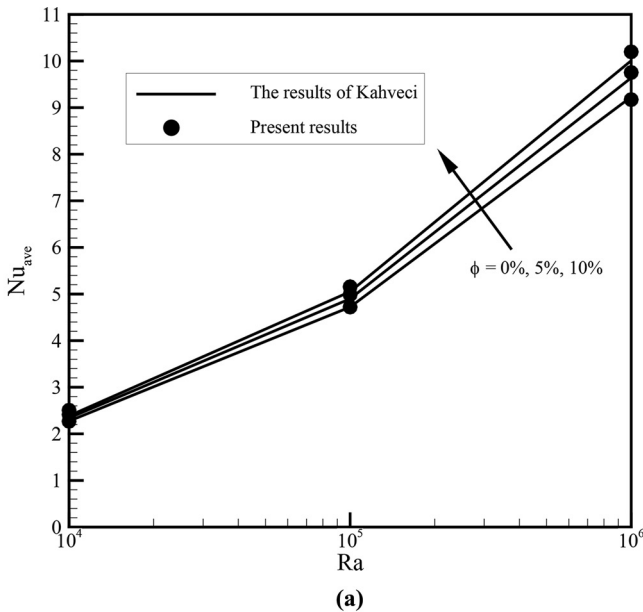


Figure 2. Current findings versus findings of (a) Kahveci (2010) (H₂O-TiO₂ nanofluid) and (b) Raisi (2016) for $n = 1.8$

Sources: Authors' work; Raisi's work (2016)

0.109433 with a rise in n from 1.5 to 1.8. The warmed stream close to the hot baffles with lower density may move uphill owing to buoyancy. Accordingly, the stream may miss its temperature near the cold walls and ribs, which may cause circulation areas. The U exhibits rotated circulation areas that are counter-clockwise in the region adjacent to the upper hot baffle and clockwise rotated circulation zones in the area contiguous to the lower hot baffle

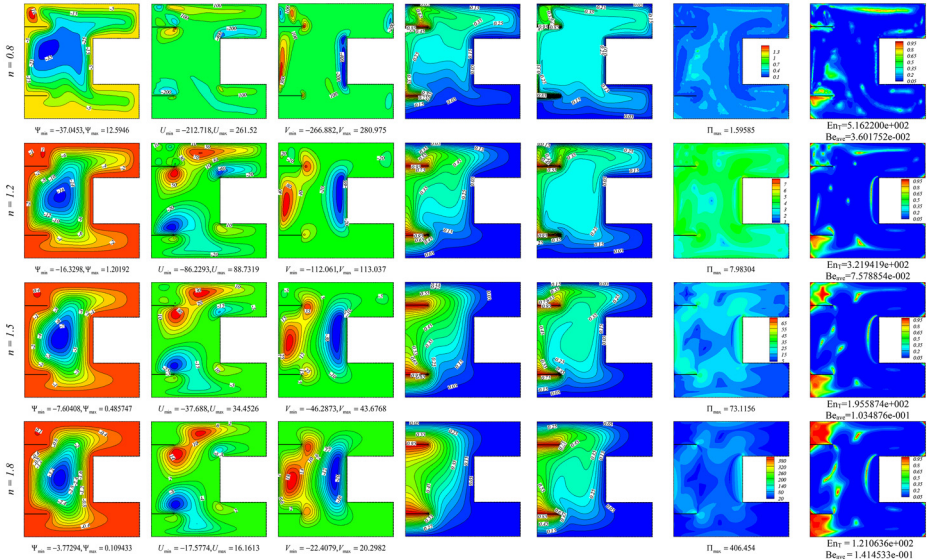


Figure 3. Dependence of Ψ , velocities, θ , C , Π , Be_{local} , Be_{ave} and En_T on n ($Le = 5$, $Ha = 0$, $N = 1$, $Ra = 10^6$, $\phi = 2\%$, Model I)

Source: Authors' work

at n of 1.2. Both clockwise and counter-clockwise rotated circulation zones cover the regions in the lower and upper arms of the domain, respectively. Such circulation zones may well be parallel to the upper and lower cold surfaces of the domain. Besides, secondary rotated circulation areas that are clockwise can be formed near the upper wall of the cold rib, while counter-clockwise ones may be created near the lower wall of the cold rib within the cavity. Exactly similar x -direction velocity patterns but with less distortion are visualized at $n = 1.5$ and 1.8. The minimum and maximum U regions occupy a considerable area of a C-shaped domain. The absolute figure of the upper limit of x -direction velocity ($|U_{max}|$) is 261.52 at $n = 0.8$. When n ameliorates from 0.8 to 1.2, or from 1.2 to 1.5, or from 1.5 to 1.8, a substantial diminution of U is envisaged. $|U_{max}|$ decreases by 66.07%, 61.17% and 53.09%, respectively, with increasing n from 0.8 to 1.2, 1.2 to 1.5 and 1.5 to 1.8, respectively. Identically, the V may exhibit two circulation areas of opposite orientations: clockwise-oriented circulation zones at the cold rib and counter-clockwise oriented circulation zones at hot baffles. When n enhances, the circulation zones are produced with more number of eyes. Further, at a higher n of 1.5 and 1.8, these two big circulation zones are accommodated in the region between hot baffles and cold ribs. The V_{min} and V_{max} may well be, respectively, 112.061 and 113.037 at $n = 1.2$. At high n of 1.5 and 1.8, the magnitudes of V_{min} and V_{max} may lessen to (46.2873, 22.4079) and (43.6768, 20.2982), respectively. The maximum V areas get more extended in the region between two baffles and are parallel to the adiabatic wall between them. Further, the minimum V zones get expanded in the region close to the cold rib and are parallel to it. These regions near the cold rib may spin in directions that are clockwise. The V notably peters out at higher n , indicating low buoyancy created a convection stream inside the cavity. The V_{min} decreases by 58.01%, 58.69% and 51.59%, respectively, because of a rise in n from 0.8 to 1.2, 1.2 to 1.5 and 1.5 to 1.8. The V_{max} decreases by 59.76%, 61.36% and 53.52%, respectively, because of rise in n from 0.8 to 1.2,

1.2 to 1.5 and 1.5 to 1.8. As far as the temperature distribution inside the cavity is concerned, it is visualized that the isotherms are lined up with the cold ribs of the cavity at lower n , which can lead the plume-like shaped isotherm to develop near baffles. Increasing n to higher amounts ($n = 1.5, 1.8$) may cause small distortions near the hot baffles and notable distortions away from the hot baffles and toward cold rib. When n rises, heat and mass transfer of dilatant fluid takes place in the shorter distance between the hot wall and cold rib. This indicates that convection of heat and mass transfer diminishes prominently with the amelioration of n . As a result, the isotherm and isoconcentration distributions of dilatant fluids decline. When n rises, Π ameliorates significantly. The maximum apparent viscosity Π_{\max} enhances by 400.23%, 815.89% and 455.9%, respectively, because of the amplification of n from 0.8 to 1.2, 1.2 to 1.5 and 1.5 to 1.8. Most local Bejan numbers are attained near the hot baffles rather than the remaining regions of the cavity for any n . However, prominent local Bejan number Be_{loc} is obtained near the hot baffles at n of 1.8. The entropy decreases by 37.63%, 39.25% and 38.10%, respectively, when n rises from 0.8 to 1.2, 1.2 to 1.5 and 1.5 to 1.8. It is noticed that the average Bejan number Be_{ave} enhances by 110.42%, 36.55% and 36.69% when n grows from 0.8 to 1.2, 1.2 to 1.5 and 1.5 to 1.8, respectively.

4.2 Influence of baffle length (L)

Figure 4 indicates the variability of streamlines, velocities, θ , concentrations, Be_{loc} , Be_{ave} and entropy generation with varied baffle length L at $Le = 5, Ha = 0, N = 1, Ra = 10^6, \phi = 2\%$ and $n = 1.5$. It is envisaged that counter-clockwise rotating streamlines may be formed in the central part of the domain for any baffle length ($0.1 \leq L \leq 0.3$). Such streamlines are parallel to the adiabatic wall between two hot baffles and the inner wall of the cold rib. The streamlines get well stretched, covering the lower and upper arms of the domain, when L grows from 0.1 to 0.2 and 0.2 to 0.3. The minimum absolute value of the streamlines ($|\psi_{\min}|$) decreases by 1.2% and 5.2%, respectively, when L grows from 0.1 to 0.2 and 0.2 to 0.3. Further, maximum value of streamlines (ψ_{\max}) exhibits a robust enhancement by $1.3 \times 10^5\%$ and minor amelioration by 4.38%, respectively, when L grows from 0.1 to 0.2 and 0.2 to 0.3. This enhancement of ψ_{\max} is because of the strong convection current caused by the more hot fluid, which is because of hot baffles of greater length within the cavity. The

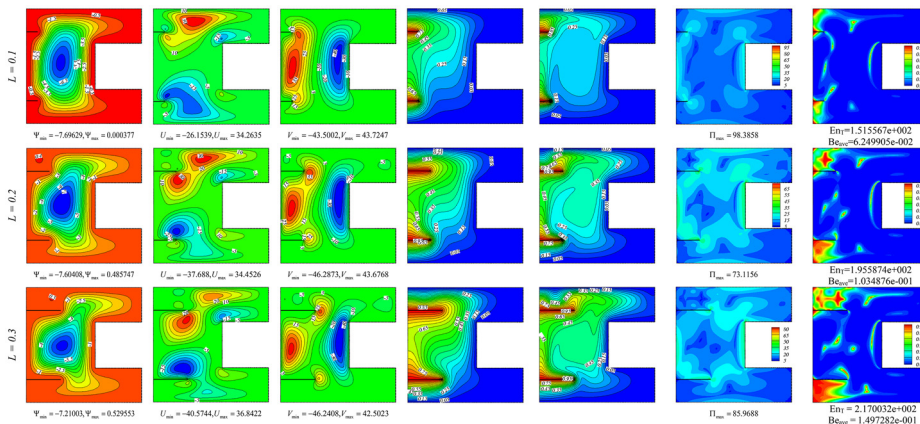


Figure 4. Dependence of Ψ , velocities, θ , C , Π , Be_{loc} , Be_{ave} and En_T on L ($Le = 5, Ha = 0, N = 1, Ra = 10^6, \phi = 2\%, n = 1.5, Model I$)

Source: Authors' work

U is represented by counter-clockwise rotating circulation areas at the upper hot baffle and clockwise rotating circulation zones at the lower hot baffle with a low baffle length L of 0.1. The U_{max} appears near the upper hot baffle, while the U_{min} may be attained adjacent to the lower hot baffle. Apart from this, the other two subsidiary circulation zones are created at the cold rib. When baffle length grows to 0.2 to 0.3, the U circulation areas get stretched significantly. The absolute minimum amount of U increases by 44% and 11.1%, respectively, when the baffle length grows from 0.1 to 0.2 and 0.2 to 0.3. Further, the maximum amount of U ameliorates marginally by 0.55% and 6.94%, respectively, when baffle length amplifies from 0.1 to 0.2 and 0.2 to 0.3. As far as y -direction velocity is concerned, they feature oppositely directed circulation zones. Maximum V circulation zones appearing at hot baffles spin in counter-clockwise directions, while minimum V circulation zones visible at cold ribs spin in clockwise directions. The absolute maximum value of V increases marginally by 0.64% and 0.33%, respectively, when baffle length increases from 0.1 to 0.2 and 0.2 to 0.3. Further, maximum V attains subtle diminution by 0.11% and 2.7%, respectively, when baffle length grows from 0.1 to 0.2 and 0.2 to 0.3. Isothermal and concentration lines are partially lined up with cold ribs for any baffle length ($0.1 \leq L \leq 0.3$). Further, isothermal and concentration lines are significantly more distorted, indicating intensified θ and concentration distributions because of the growth of baffle length from 0.1 to 0.2 and 0.2 to 0.3. In fact, when baffle length increases, the thermal expansion of nanofluid will increase. As a result, thermal and solutal buoyancy forces increase, thereby intensifying both thermal and mass diffusions. At low L , the entire cavity is accommodated by low apparent viscosity Π , where least Π_{max} is recorded as 7.98304. When baffle length L increases, the region inside the cavity occupies the low and moderate values of apparent viscosity. However, Π_{max} reduces by 25.68% and enhances by 17.58%, respectively, because of a rise in L from 0.1 to 0.2 and 0.2 to 0.3. The entropy decreases by 29.1% and 10.95%, respectively, when L rises from 0.1 to 0.2 and 0.2 to 0.3. It is noticed that the average Bejan number Be_{ave} enhances by 66.58% and 44.68% when L grows from 0.1 to 0.2 and 0.2 to 0.3, respectively.

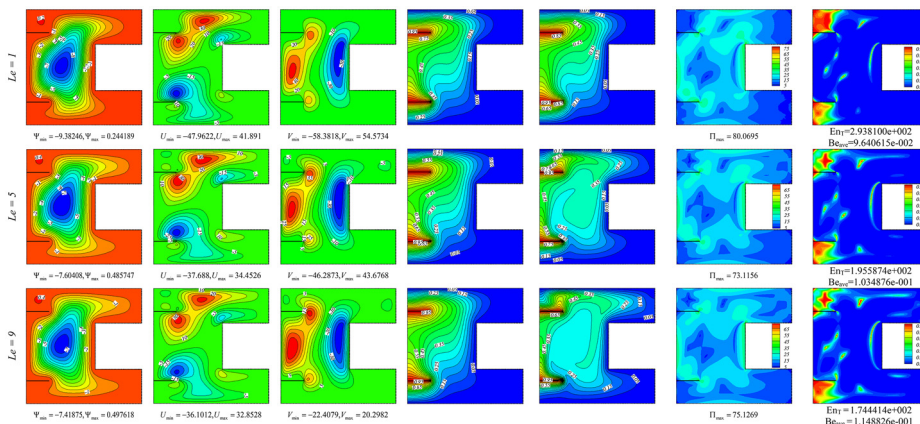
4.3 Influence of Lewis number (Le)

Figure 5 shows the variability of streamlines, velocities, θ , concentrations, Be_{loc} , Be_{ave} and entropy generation with varied Lewis numbers Le at $Ha = 0$, $N = 1$, $Ra = 10^6$, $\phi = 2\%$ and $n = 1.5$. It is envisaged that clockwise rotating streamlines are produced in the region between hot baffles and the cold rib of the cavity at a low Lewis number. Such streamlines are partially lined up with the adiabatic wall between two hot baffles and the inner wall of the cold rib. The minimum and maximum amounts of stream function are -9.38246 and 0.244189 , respectively, at low Le of 1. When Le enhances from 1 to 5 and 5 to 9, the streamlines get stretched well, indicating their intensification. The minimum absolute value of the streamlines ($|\psi_{min}|$) decreases by 18.95% and 2.44%, respectively, when L grows from 1 to 5 and 5 to 9. Further, maximum value of streamlines (ψ_{max}) enhances by 98.92% and 2.44%, respectively, when L grows from 1 to 5 and 5 to 9. In this environment, simultaneous heat and mass transfer because of the flow of nanofluid takes place. When Le rises, thermal transport dominates over mass transport, indicating a greater convection current. As a consequence, ψ_{max} enhances. The U is represented by counter-clockwise rotating circulation areas at the upper hot baffle, indicating the maximum velocity region, while clockwise rotating circulation zones at the lower hot baffle indicate the minimum velocity region with a low Le of 1. Additionally, the other two secondary circulation zones are developed at the cold rib. When Le increases from 1 to 5 and 5 to 9, the absolute minimum value of U decreases by 21.42% and 4.21%, respectively. Further, the maximum amount of U increases

by 17.76% and 4.64%, respectively, when Le grows from 1 to 5 and 5 to 9. Further, circulation areas related to V are featured with oppositely directed circulation zones. Maximum V zones rotating in counter-clock-wise directions appear at hot baffles, while minimum V areas rotating in clockwise directions are visualized at cold ribs. The absolute minimum value of y-direction velocity emaciates by 20.72% and 51.59%, respectively, when Le increases from 1 to 5 and 5 to 9. Further, maximum V decreases by 19.97% and 53.53%, respectively, when Le increases from 1 to 5 and 5 to 9. Partially lined up with a cold rib, density of isothermal and isoconcentration lines grows with an increase in Lewis number, indicating intensified temperature and concentration distributions. This implies that thermal and solutal stratifications take place in the gap between hot baffles and cold ribs because of more thermal and solutal penetrations. This led to the formation of thermal and solutal boundary layers along the cold walls and cold ribs. At low Le , the apparent viscosity Π is the highest (80.0695) among all the values of Le . When Le increases from 1 to 5, Π_{\max} reduces by 8.7% and enhances by 2.8% because of a rise in Le from 5 to 9. The entropy decreases by 33.43 and 10.81%, respectively, when Le rises from 1 to 5 and 5 to 9. At low Le of value 1, localized Bejan number Be_{loc} becomes maximum above the upper hot baffle and below the lower hot baffle. The majority of the cavity is accommodated by a minimum Be_{loc} . It is observed that Be_{ave} enhances by 7.34% and 11.01%, respectively, when Le rises from 1 to 5 and 5 to 9.

4.4 Influence of buoyancy ratio (N)

Figure 6 reveals the variability of streamlines, velocities, θ , concentrations, Be_{loc} , Be_{ave} and entropy generation with varied buoyancy ratio N at $n = 1.5$, $Ha = 0$, $Le = 5$, $Ra = 10^6$ and $\phi = 2\%$. At $N = 1$, which is under the identical influence of solutal and thermal buoyancies, clock-wise rotating circular zones with egg-shaped eyes are formed in the central area of the domain. The minimum and maximum figures of stream function are -7.60408 and 0.485747 , respectively, at a low Na of 1. When N enhances from 1 to 3, streamlines/circulation zones get stretched; however, ψ_{\min} and ψ_{\max} decrease in their values. With a further increase in N from 3 to 5, streamlines ameliorate because of greater thermal buoyancy compared to solutal buoyancy. Further, ψ_{\min} and ψ_{\max} show an opposite trend with a rise of N from 3 to 5. The x-direction velocity profiles feature two oppositely oriented



Source: Authors' work

Figure 5. Dependence of Ψ , velocities, θ , C , Π , Be_{local} , Be_{ave} and Ent_T on Le ($n = 1.5$, $Ha = 0$, $N = 1$, $Ra = 10^6$, $\phi = 2\%$, Model I)

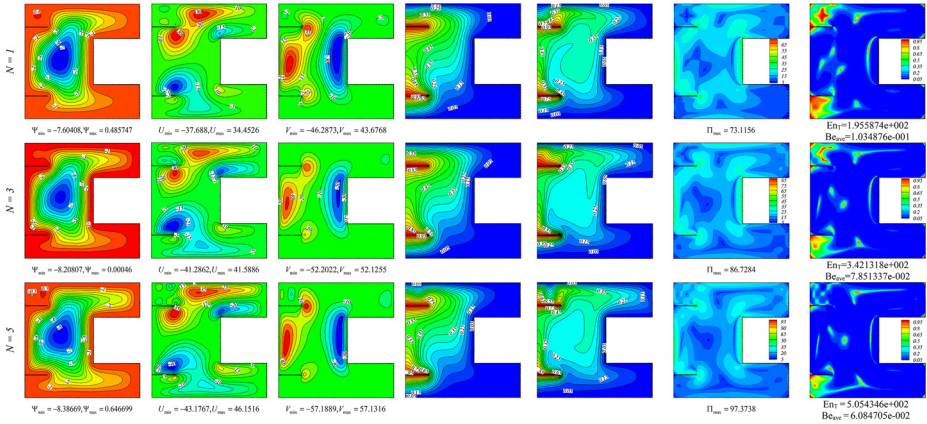


Figure 6. Dependence of Ψ , velocities, θ , C , Π , Be_{local} , Be_{ave} and En_T on N ($n = 1.5$, $Ha = 0$, $Le = 5$, $Ra = 10^6$, $\phi = 2\%$, Model I)

Source: Authors' work

primary circulation zones at the hot baffles, along with two subsidiary circulation zones at the cold rib. The maximum U areas are visualized near the hot baffles, while the minimum U parts are envisaged near the cold rib. At a low buoyancy ratio N of 1, minimum and maximum x -direction velocities are, respectively, -37.688 and 34.4526 . Further, the absolute of minimum x -direction velocity $|U_{min}|$ enhances by 9.55% and 4.58%, respectively, when N increases from 1 to 3 and 3 to 5. In addition, maximum x -direction velocity $|U_{max}|$ enhances by 20.71% and 10.97%, respectively, when N increases from 1 to 3 and 3 to 5. The y -direction velocity V is manifested by circulation zones of counter-clockwise rotations at hot baffles and those of clockwise rotations at cold ribs. There is a prominent amelioration of y -direction velocity with a rise in N from 1 to 3 and 3 to 5. It is noticed that $|V_{min}|$ enhances by 12.41% and 9.55%, respectively, with a rise in N from 1 to 3 and 3 to 5. Further, V_{max} increases by 19.34% and 9.96%, respectively, with the same rise in N . It is noticeable that a rise in buoyancy ratio leads to a significant augmentation of the gradient of isotherms on the hot wall. This implies that a rise in buoyancy ratio accounts for ameliorating heat transfer. A similar trend is envisaged in isoconcentration, where their gradient enhances prominently. Consequently, mass transfer, similar to heat transfer, is improved by enhancing the buoyancy ratio. At low N , apparent viscosity Π is the lowest (73.1156) among all the values of N . When N increases from 1 to 3, Π_{max} ameliorates by 18.62% and 12.27% because of a rise in N from 3 to 5. The entropy increases by 74.92% and 47.73%, respectively, when N rises from 1 to 3 and 3 to 5. The localized Bejan number reaches its maximum above the upper hot baffle and below the lower hot baffle at a low N of 1. The majority of the cavity is catered to by minimum Be_{loc} . It is noticed that Be_{ave} exhibits a reduction by 24.13% and 22.5% when N rises from 1 to 3 and 3 to 5.

4.5 Influence of Hartmann number (Ha)

Figure 7 shows the variability of streamlines, velocities, θ , concentrations, Be_{loc} , Be_{ave} and entropy generation with different Ha at $n = 1.5$, $N = 1$, $Le = 5$, $Ra = 10^6$, $\phi = 2\%$. At $Ha = 0$, the rotating circulation areas of higher magnitude, which are clockwise, can be constructed in the district between hot baffles, cold ribs and the lower and upper arms of the cavity, while counter-clockwise ones of lower magnitude may be developed in this zone. Streamlines may well be lined up with the adiabatic wall between hot baffles and with the

cold rib of the cavity. Circulation zones are symmetric in nature at both low and high values of Ha . By growing Ha , the circulation zones of the flow of nanofluid were dragged toward the cold rib of the cavity. This behavior resulted in the weakening of the zones compared to the zones in the central region of the cavity. This implies that flow velocity peters out. In the case of magnetic efficacy, circulation areas of low magnitude may present low distortion in comparison to $Ha = 0$ because of the Lorentz force that barricades convection stream, thereby lessening the streamlines' distortion. Physically, higher Ha may boost the Lorentz force, which can result in the suppression of the convection flow. When the situation is switched over from hydrodynamic to MHD influence, the minimum and maximum streamlines whittle down by 12.7% and 7.12%, respectively. The U may present two circulation areas of maximum and minimum U near the upper and lower hot baffles, respectively. The counter-clock-wise rotated circulation zones appearing at the upper hot baffle indicate the maximum x -direction velocity region, while the clockwise rotated circulation parts appearing at the lower hot baffle represent the minimum x -direction velocity. Apart from this, a few secondary circulation parts of minimum U are visualized near the cold rib. A magnetic field won't alter the structure of the minimum and maximum U zones. The presence of a magnetic field makes absolute minimum and maximum amount of U reduction by 6.8% and 8.1%, respectively. The V 's distribution displays that the maximum velocity parts – spinning in counter-clockwise directions – get expanded and lined up along the adiabatic wall between the hot baffles. However, the minimum velocity parts rotating in clockwise directions may be lined up along the cold rib. The absolute V_{min} and V_{max} peter out by 10.44% and 8.51%, respectively, when the magnetic field influence comes into play. The magnitude of velocity distributions diminished with the increase in Ha . The phenomenon indicates that amelioration of the Hartmann number increases the Lorentz force, thereby weakening the convection process. Isotherms at $Ha = 0$ present maximum distortions, while these distortions may be lessened by considering the magnetic field. As Ha grows, the temperature distribution of non-Newtonian power law nanofluids reduces. It is a fact that the rise in Ha leads to a diminution in the gradient of isotherms on a hot wall. This trend implies that the convection process becomes weaker with an amelioration of the Hartmann number. The distribution of isoconcentration between the hot surface and the cold rib declines as Ha rises. This confirms that mass transfer may lessen with Ha 's growth. The apparent viscosity decreases by increasing the Ha number. It is clear that the maximum apparent viscosity Π_{max} drops by 2.9% when Ha rises from 0 to 40. Entropy generation En_T decays by 0.33% because of the growth of Ha from 0 to 40. The maximum Be_{loc} appears in the region above the upper hot baffle and below the lower hot baffle, while other regions of the cavity accommodate moderate and minimum values of Be_{loc} in the absence as well as the

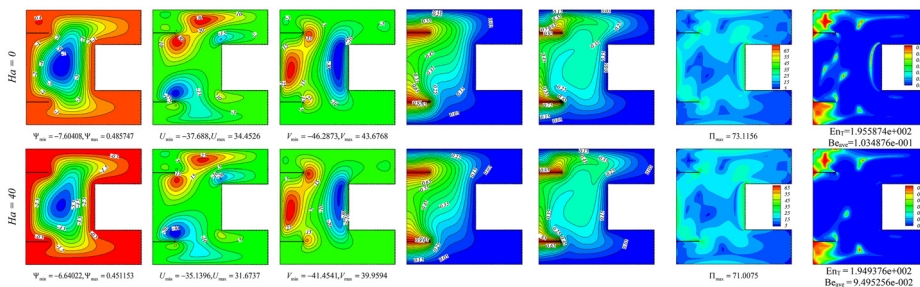


Figure 7. Dependence of Ψ , velocities, θ , C , Π , Be_{local} , Be_{ave} and En_T on Ha ($n = 1.5$, $N = 1$, $Le = 5$, $Ra = 10^6$, $\phi = 2\%$, Model I)

Source: Authors' work

presence of a magnetic field. When Ha increases, the average Be drops by 8.25%, owing to the development of a low convection stream.

4.6 Influence of Raleigh number (Ra)

Figure 8 manifests the impact of the Rayleigh number on streamlines, velocities, isotherms, concentrations, entropy generation and local and average Be for $n = 1.5, N = 1, Le = 5, Ha = 0$ and $\phi = 2\%$. The first column of Figure 8 indicates streamlines for $Ra = 10^5$ and 10^6 . Clockwise rotating circulation zones are visualized inside the cavity. The center of circulation zones appears near the middle of the cavity. The circulation zones get stretched in the narrow regions of the domain when Ra increases from 10^5 to 10^6 . The shape of circular zones is because of the thermal buoyant force generated by the hot baffles. Nanofluid within the cavity gets heated by the hot baffles, and the density of the nanofluid becomes lower adjacent to the hot baffles. As a consequence, nanofluid close to the hot baffles becomes lighter, which in turn moves upward toward the upper cold surface and cold rib. In contrast, nanofluid adjacent to the cold wall and cold rib is of higher density compared to that near the hot baffles. Because of its higher density, nanofluid moves downward, developing clockwise circulations within the cavity. This trend of downward motion is more prominent near the cold rib than the cold wall of the cavity. Because of the impotent buoyancy-induced convection stream because of the low Ra , distortions in the streamlines cannot be visualized. But ascending the Ra to 10^6 may yield significant distortions in streamlines, which means circulations grow in size and elongate toward the cold walls because of the higher temperature difference between the hot baffles and cold walls. The strength of circulation zones increases with a rise in Rayleigh numbers from 10^5 to 10^6 . Moreover, streamlines are of higher strength near the middle of the cavity for any value of Ra . This is because of the higher thermal conductivity of nanofluid. The strength of minimum circulation zones enhances by 187.81% and that of maximum circulation zones ameliorate by 512.2% respectively when Ra rises from 10^5 to 10^6 . The U may exhibit rotated circulation parts that are counter-clockwise at the top hot baffle, while clockwise ones can be observed at the bottom hot baffle at Ra of 10^5 . The minimum U may be attained in the lower arm of the cavity and above the lower hot baffle. A remarkable growth in U is visualized with a rise in Ra . The absolute amount of minimum U enhances by 210.88% and maximum U enhances by 211.04% by growing the Ra from 10^5 to 10^6 . This is because of amplified buoyancy creating a convection stream in the domain. When Ra grows, apart from the bigger circulation zones, two secondary zones are produced at the cold rib. The maximum-minimum V parts spread out in bulk of the cavity. The V_{min} and V_{max} are, respectively, -15.4568 and 18.6464 at $Ra = 10^5$. These may rise by 199.5% and 219.84% respectively by

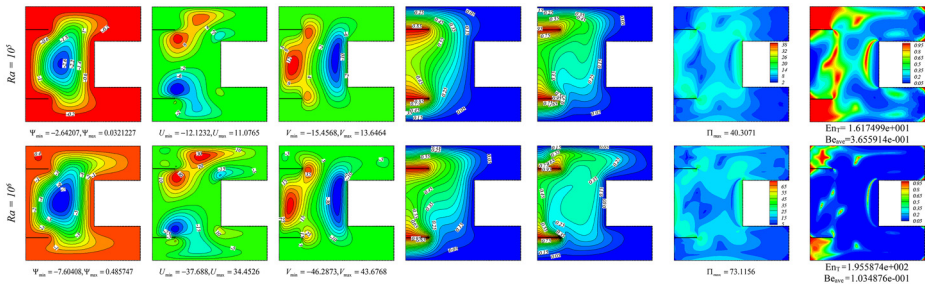


Figure 8. Dependence of Ψ , velocities, θ , C , Π , Be_{local} , Be_{ave} and En_T on Ra ($n = 1.5, N = 1, Le = 5, Ha = 0, \phi = 2\%$, Model I)

Source: Authors' work

growing Ra from 10^5 to 10^6 . The V_{max} parts get more expanded toward the cold rib and the cold walls, while the V_{min} areas get more extended toward the central region and the cold walls of the cavity compared to the case in which Ra is lower. As far as the temperature distribution inside the cavity is concerned, it may be noted that the isotherms are nearly parallel near the hot baffles and cold rib at $Ra = 10^5$, indicating the development of thermal boundary layers near the hot baffles and the cold rib. At lower Ra , plume-like shaped isotherms can be formed near the hot baffles, and there may be minimal distortion in this case for the isotherms. Ascending Ra to 10^6 may cause significantly greater distortion near the middle of the cavity, showing evidence of increased convection. This implies that amplified temperature distributions may well be owing to the almost higher convection stream induced at high Ra in the presence of nanofluid. The concentration distribution inside the cavity shows that they are dense near the hot baffles and spread slowly toward the upper and lower arms and cold rib, showing minimum distortion at low Ra . They are nearly parallel at the cold rib. When Ra numbers increase, the concentrations get more distorted and occupy almost the entire region of the cavity, indicating a higher mass diffusivity of nanoparticles. The apparent viscosity is ameliorated by increasing the Ra number. It is noticed that Π_{max} increases by 81.4% when Ra rises from 10^5 to 10^6 . Entropy generation En_T uplifts by 1109.2% because of the growth of Ra from 10^5 to 10^6 . The maximum Be_{loc} appears in the left top and left bottom corners of the cavity, while the other regions of the cavity accommodate the moderate and minimum amounts of Bejan numbers at low Ra numbers. When Ra increases, the major part of the cavity accommodates the minimum value of Be_{loc} , implicating a lower Be_{loc} . The Be_{ave} reduces by 71.7% because of the development of a high convection stream from hot baffles toward the cold walls and cold ribs of the cavity.

4.7 Influence of Le , n , N , Ra , Ha and L on Nusselt numbers

The variation of the local Nusselt number Nu_{loc} and average Nusselt number Nu_{ave} in response to sundry Le , n , N , Ra , Ha and L is delineated in Figure 9. It is understood that the local Nusselt number Nu_{loc} decreases with a rise in Le . However, the decrease is unnoticeable when Le rises from 1 to 5. Such a diminution of Nu_{loc} is prominent at the moderate length of the cold rib. At fixed Le (say, $Le = 1$), Nu_{loc} was nil at the very low length of the cold rib S , then increased exponentially with the gradual growth of S . Nu_{loc} is then decreased with further rise in S . At moderate S , Nu_{loc} enhances sharply and then attains the highest value, followed by an exponential descending trend for the longer length of the cold rib. Further, the average Nusselt number Nu_{ave} decreases by 8.4% and 0.8%, respectively, when Le rises from 1 to 5 and 5 to 9. However, the diminution of Nu_{ave} is marginal. When the power-law index n rises, Nu_{loc} uplifts and attains its maximum value. With further increases in S , Nu_{loc} follows an ascending trend, attains the largest value at high S and then decreases with further growth in S . Other values of n contribute to a similar trend of enhancement of Nu_{loc} compared to that of 0.8. It is clear that when n increases, Nu_{loc} reduces for any S . Further, Nu_{ave} decreases by 53.44%, 30.33% and 19.36% when n rises from 0.8 to 1.2, 1.2 to 1.5 and 1.5 to 1.8, respectively. Nu_{loc} shows subtle variation in the rise in buoyancy ratio N for any length of the cold rib. Two peaks of the Nu_{loc} profiles indicate that it attains the two maximum values at two specific lengths of the cold rib. When S grows, Nu_{loc} enhances and attains its first maximum value, then decreases, followed by an ascending trend, thereby attending the second maximum, further followed by a descending trend. The variation of Nu_{loc} is insignificant with the rise in N . Further, Nu_{ave} enhances by 0.82% and 0.34%, respectively, when N rises from 1 to 2 and 2 to 3. It is obvious that the heat transfer rate uplifts because of the rise in Rayleigh number Ra against S . The highest Nu_{loc} is attained at

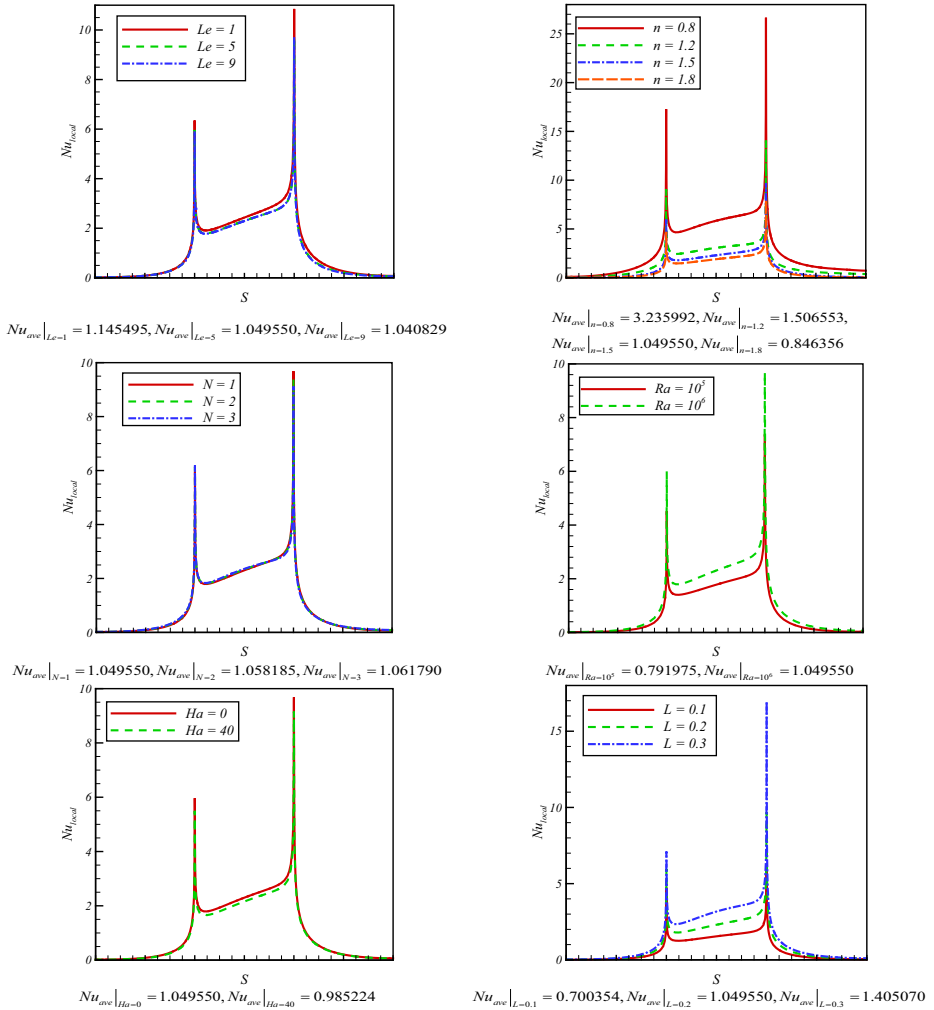


Figure 9.
Nu's alteration with
active parameters
(Model I)

Source: Authors' work

high Ra ($Ra = 10^6$) and high S. Further, Nu_{ave} increases by 32.52% when Ra rises from 10^5 to 10^6 . Considering magnetic efficacy, Nu_{loc} was higher compared to that in the presence of the magnetic field, whatever the length of the cold rib may be. Further, Nu_{ave} reduces by 6.13% under the influence of the magnetic field. Finally, Nu_{loc} upgrades because of the rise in length of hot baffles in a specific range of lengths of cold rib. The variation of Nu_{loc} is prominent at the moderate length of the cold rib. Further, Nu_{loc} attains two maximum values for a greater length of hot baffles ($L = 0.3$) at a specific length of the cold rib of the cavity. It is seen that Nu_{ave} enhances by 49.86% and 33.87%, respectively, when L grows from 0.1 to 0.2 and 0.2 to 0.3.

4.8 Influence of Le , n , N , Ra , Ha and L on local and average Sherwood numbers

Figure 10 manifests the variations of local and average Sherwood numbers under the impact of Le , n , N , Ra , Ha and L at different lengths of cold rib. It is visualized that the local Sherwood number Sh_{loc} intensifies prominently with a rise in Le ($Le = 1, 5, 9$) at the disparate length of the cold rib. At the lower length of the cold rib, Sh_{loc} exhibits an ascending trend; at the moderate length of the cold rib, it exhibits an uptrend and a descending trend at the larger length of the cold rib. Two maximum values of Sh_{loc} are attained at high Le at two specific values of S . Further, Sh_{loc} increases substantially by 73.97% and 23.715, respectively, when Le rises from 1 to 5 and 5 to 9. The Sh_{loc} emaciates

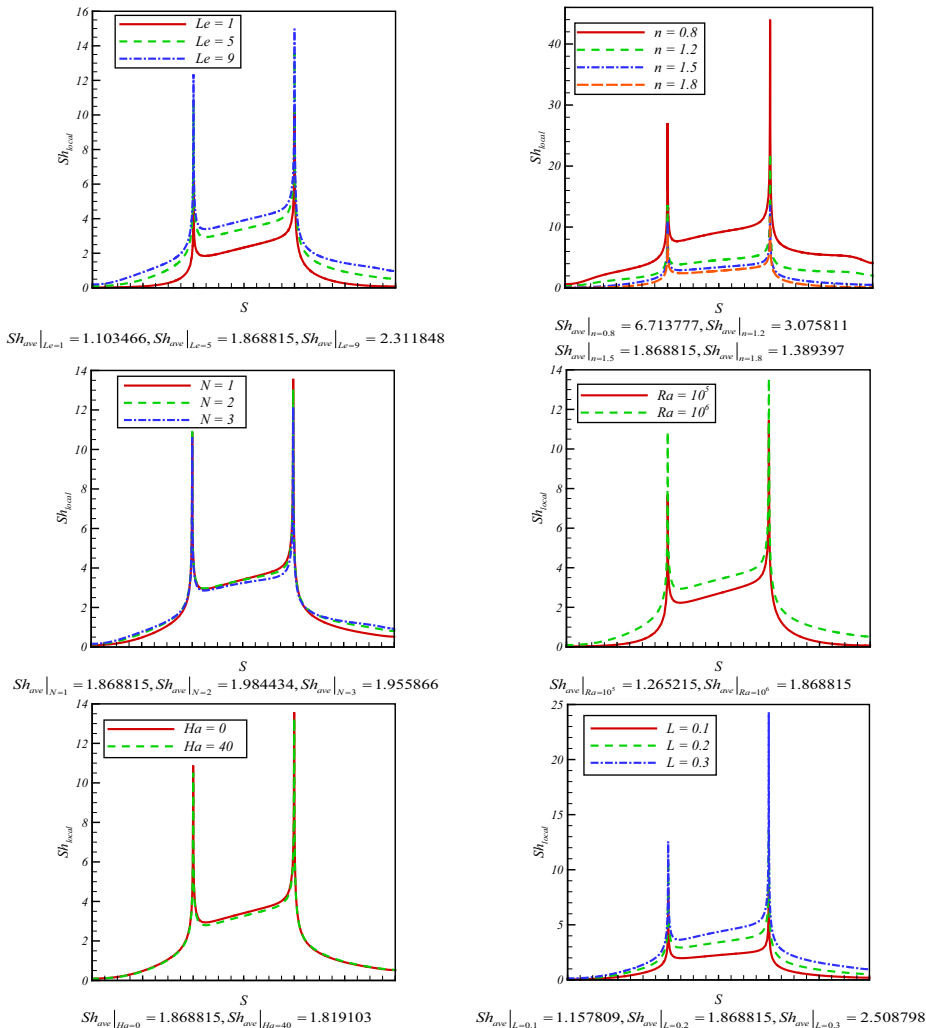


Figure 10.
Sh's alteration with
active parameters
(Model I)

Source: Authors' work

significantly with rise in n ($n = 0.8, 1.2, 1.5$ and 1.8), irrespective of the length of the cold rib of the C-shaped cavity. Again, Sh_{loc} attains its two maximum values, indicated by two peaks at any amounts of power-law index at specific lengths of the cold rib. It is estimated that Sh_{ave} decreases by 54.18% when n rises from 0.8 to 1.2 and 39.24% when n rises from 1.2 to 1.5, while that increases by 25.65% with a rise of n from 1.5 to 1.8. The rise of N leads to an enhancement of mass transfer rate at lower and higher lengths of the cold rib, while the reverse trend is visualized at moderate lengths of the cold rib. In this case, Sh_{ave} increases by 6.19% when N rises from 1 to 2, while it decreases by 1.44% (marginal diminution) with the rise of N from 2 to 3. As expected, Sh_{loc} enhances because of the rise in Ra for any suitable length of cold rib. In this case, Sh_{loc} yields two maximum values at a high Rayleigh number of 10^6 at two specific lengths of cold rib. Here, Sh_{ave} increases by 47.71% when Ra amplifies from 10^5 to 10^6 . Interestingly, Sh_{loc} variation is exactly similar to that of Nu_{loc} in the absence ($Ha = 0$) as well as in the presence of a magnetic effect ($Ha = 40$). Further, Sh_{ave} decreases by 2.66% because of the augmentation of the Hartmann number. The growth of the length of the hot baffles contributes to the rise of the local mass transfer rate at the subtle lengths of the cold ribs of the cavity. Here, Sh_{loc} attains a maximum value at a higher baffle length at a specific length of the cold rib. Further, Sh_{ave} increases by 61.45 and 34.25%, respectively, with a rise in the length of the hot baffle from 0.1 to 0.2 and 0.2 to 0.3.

Supplementary correlations (Model II) proposed by Corcione (Corcione *et al.*, 2015; Corcione, 2011) for thermal conductivity and viscosity of nanofluids used in this research are as follows:

$$\frac{\mu_{nf}}{\mu_f} = \frac{1}{1 - 34.87\phi^{1.03} \left(\frac{d_p}{d_f}\right)^{-0.3}}$$

$$\frac{k_{nf}}{\mu_f} = 1 + 4.4Pr^{0.66} \phi^{0.66} \left(\frac{k_s}{k_f}\right)^{0.03} Re^{0.4} \left(\frac{T}{T_{fr}}\right)^{10}$$

where Re , d_p , d_f and T_{fr} indicate Reynolds number, diameter of nanoparticle, H_2O molecule's diameter and base liquid's freezing point, respectively. Figure 11 displays the comparative study of Ψ , velocities, θ , C , Π , Be_{ave} and En_T for Models I and II. From the comparison it is obvious that the shape, structure and strength of the streamlines, horizontal and vertical velocities, isotherms, isoconcentrations, apparent viscosity, entropy generation and average Bejan number of Models I and II are nearly the same. Table 2 exhibits the comparative study of Nu_{ave} and Sh_{ave} for different ϕ of Models I and II. It may well be interesting to note that

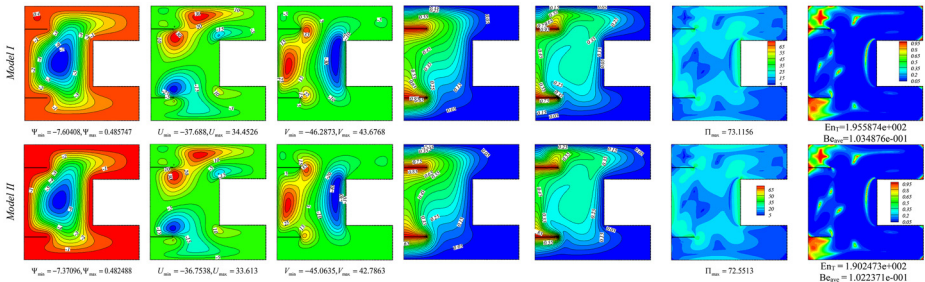


Figure 11. Ψ , velocities, θ , C , Π , Be_{ave} and En_T for Models I and II ($n = 1.5, N = 1, Le = 5, Ha = 0, \phi = 2\%, Ra = 10^6$)

Source: Authors' work

for Model II, the average Nu may possess a reduction trend with growing ϕ , which is reverse for Model I.

5. Conclusions

In this work, the second law and thermal behavior of non-Newtonian DDNC of $Al_2O_3-H_2O$ NF within a C-shaped domain with two hot baffles located in the left wall and impacted by a magnetic field were investigated. The governing equations have been solved using the FEM. The effects of conjugate buoyancies and MHDs have been studied. Some of the major outcomes of the present study are as follows:

- It is clear to convey that increasing n to 1.2, 1.5 and 1.8 may yield a small distortion in streamlines near the cold walls and cold ribs of the cavity. When n ameliorates from 0.8 to 1.2, 1.2 to 1.5 and 1.5 to 1.8, $|U_{max}|$ decreases substantially by 66.07%, 61.17% and 53.09%, respectively. The minimum y -direction velocity decreases by 58.01%, 58.69% and 51.59%, while the maximum of that velocity decreases by 59.76%, 61.36% and 53.52%, respectively, because of the rise in n from 0.8 to 1.2, 1.2 to 1.5 and 1.5 to 1.8. The amplified temperature distributions may be owing to relatively high convection currents. When n rises, Π ameliorates significantly. The entropy decreases by 37.63%, 39.25% and 38.10%, and the average Bejan number Be_{ave} enhances by 110.42%, 36.55% and 36.69% when n grows from 0.8 to 1.2, 1.2 to 1.5 and 1.5 to 1.8, respectively.
- As observed, the rise in L leads to an intensification of streamlines. The maximum x -direction velocity appears near the upper hot baffle, while the minimum U is attained adjacent to the lower hot baffle. The maximum amount of U ameliorates marginally by 0.55% and 6.94%, respectively, when baffle length L amplifies from 0.1 to 0.2 and 0.2 to 0.3. Isothermal and concentration lines are significantly more distorted, indicating intensified temperature and concentration distributions because of the growth of baffle length. In addition, when L grows from 0.1 to 0.2 and 0.2 to 0.3, respectively, Π_{max} reduces by 25.68% and enhances by 17.58%, entropy grows by 29.1% and 10.95% and Be_{ave} enhances by 65.58% and 44.68%.
- As found, ψ_{max} enhances with a rise in Le . When Le increases from 1 to 5, the absolute minimum value of x - and y -direction velocities peters out by 21.42% and 20.72%, respectively, while that reduces by 4.21% and 51.59% with a rise in Le from 5 to 9. Further, the maximum values of x - and y -direction velocities ameliorate by 17.76% and 19.97%, respectively, as Le increases from 1 to 5, while they yield the opposite trend with an increase in Le from 5 to 9. In addition, entropy lessens by 33.43% and 10.81%, while Be_{ave} grows by 7.34% and 11.01% as Le rises from 1 to 5 and 5 to 9, respectively.

ϕ (%)	Model I		Model II	
	Nu_{ave}	Sh_{ave}	Nu_{ave}	Sh_{ave}
0	0.7629719	1.296874	0.7629719	1.296874
2	0.7919716	1.265215	0.7475024	1.255157
4	0.8277270	1.214536	0.7316645	1.204787

Table 2.
Average Nu and Sh's
variation with ϕ for
different models

Source: Authors' work

- It is visualized that ψ_{\min} and ψ_{\max} decrease in their values while Π_{\max} ameliorates because of an increase in buoyancy ratio. Further, $|U_{\max}|$ enhances by 20.71% and 10.97%, while $|V_{\min}|$ enhances by 12.41% and 9.55%, respectively, when N increases from 1 to 3 and 3 to 5.
- When the situation is switched over from hydrodynamic to MHD influence, the minimum and maximum streamlines whittle down by 12.7% and 7.12%, respectively. The presence of a magnetic field causes the absolute minimum and maximum values of x - and y -direction velocities' reduction by (6.8%, 10.44%) and (8.1%, 8.51%), respectively. When Ha amplifies, the Be_{ave} lessens by 8.25%.
- The strength of minimum circulation zones enhances by 187.81% and that of maximum circulation zones ameliorates by 512.2%, respectively, when Ra rises from 10^5 to 10^6 . The absolute values of U_{\min} and U_{\max} may increase by 210.88% and 211.04%, respectively, while V_{\min} and V_{\max} may increase by 199.5% and 219.84%, respectively, by increasing the Ra from 10^5 to 10^6 . Intensified temperature and concentration distributions are accomplished at higher Ra numbers, subject to the presence of nanofluid. It is found that Π_{\max} enhances by 81.4% and En_T uplifts by 1109.2% because of the growth of Ra from 10^5 to 10^6 .
- Local Nusselt number Nu_{loc} decreases with a rise in Le and S . Further, the average Nusselt number Nu_{ave} decreases by 8.4% and 0.8%, while it enhances by 49.86% and 33.87%, respectively, when L grows from 0.1 to 0.2 and 0.2 to 0.3. In addition, Nu_{ave} decreases with a rise in n .
- It is visualized that the local Sherwood number Sh_{loc} intensifies prominently with rise in Le at disparate length of cold rib. The Sh_{loc} emaciates significantly with a rise in n , irrespective of the lengths of the cold rib of the C-shaped cavity. The rise of N leads to an enhancement of mass transfer rate at lower and higher lengths of the cold rib, while the reverse trend is visualized at moderate lengths of the cold rib. Further, Sh_{loc} increases by 73.97% and 23.715%, respectively, when Le rises from 1 to 5 and 5 to 9, while that increases by 61.45% and 34.25%, respectively, with the rise of the length of the hot baffle from 0.1 to 0.2 and 0.2 to 0.3. The additional information is that Sh_{ave} decreases by 2.66% because of the impact of a magnetic field.

References

- Al-Farhany, K., Alomari, M.A., Biswas, N., Laouer, A., Abed, A.M. and Sridhar, W. (2023), "Magnetohydrodynamic double-diffusive mixed convection in a curvilinear cavity filled with nanofluid and containing conducting fins", *International Communications in Heat and Mass Transfer*, Vol. 144, p. 106802.
- Alomari, M.A., Al-Farhany, K., Said, N.M. and Flayyih, M.A. (2022), "Numerical investigation of double-diffusive mixed convection in a split lid-driven curvilinear cavity", *International Communications in Heat and Mass Transfer*, Vol. 138, p. 106322.
- Álvarez, M., Colmenares, E. and Sequeira, F.A. (2022), "Analysis of a semi-augmented mixed finite element method for double-diffusive natural convection in porous media", *Computers and Mathematics with Applications*, Vol. 114, pp. 112-131.
- Aly, A.M. and Alsedais, N. (2023), "Natural convection of NEPCM in a partial porous H-shaped cavity: ISPH simulation", *International Journal of Numerical Methods for Heat and Fluid Flow*, Vol. 33 No. 6, pp. 2232-2249.

- Aly, A.M. and Asai, M. (2016), "ISPH method for double-diffusive natural convection under cross-diffusion effects in an anisotropic porous cavity/annulus", *International Journal of Numerical Methods for Heat and Fluid Flow*, Vol. 26 No. 1, pp. 235-268.
- Aly, A.M., Mohamed, E.M. and Alsedais, N. (2021), "Double-diffusive convection from a rotating rectangle in a finned cavity filled by a nanofluid and affected by a magnetic field", *International Communications in Heat and Mass Transfer*, Vol. 126, p. 105363.
- Awais, M., Saad, M., Ayaz, H., Ehsan, M.M. and Bhuiyan, A.A. (2020), "Computational assessment of Nano-particulate (Al₂O₃/water) utilization for enhancement of heat transfer with varying straight section lengths in a serpentine tube heat exchanger", *Thermal Science and Engineering Progress*, Vol. 20, p. 100521.
- Basak, T., Roy, S., Paul, T. and Pop, I. (2006), "Natural convection in a square cavity filled with a porous medium: effects of various thermal boundary conditions", *International Journal of Heat and Mass Transfer*, Vol. 49 Nos 7/8, pp. 1430-1441.
- Biswas, N., Mandal, D.K., Manna, N.K., Gorla, R.S.R. and Chamkha, A.J. (2023), "Hybridized nanofluidic convection in umbrella-shaped porous thermal systems with identical heating and cooling surfaces", *International Journal of Numerical Methods for Heat and Fluid Flow*, Vol. 33 No. 9, pp. 3164-3201.
- Choi, S.U. and Eastman, J.A. (1995), "Enhancing thermal conductivity of fluids with nanoparticles", (No. ANL/MSD/CP-84938; CONF-951135-29), Argonne National Lab.(ANL), Argonne, IL (United States).
- Corcione, M. (2011), "Empirical correlating equations for predicting the effective thermal conductivity and dynamic viscosity of nanofluids", *Energy Conversion and Management*, Vol. 52 No. 1, pp. 789-793.
- Corcione, M., Cianfrini, M. and Quintino, A. (2015), "Natural convection in square enclosures differentially heated at sides using alumina-water nanofluids with temperature-dependent physical properties", *Thermal Science*, Vol. 19 No. 2, pp. 591-608.
- Dogonchi, A.S., Nayak, M.K., Karimi, N., Chamkha, A.J. and Ganji, D.D. (2020), "Numerical simulation of hydrothermal features of Cu-H₂O nanofluid natural convection within a porous annulus considering diverse configurations of heater", *Journal of Thermal Analysis and Calorimetry*, Vol. 141 No. 5, pp. 2109-2125.
- Ghernoug, C., Djezzar, M., Naji, H. and Bouras, A. (2016), "Towards numerical computation of double-diffusive natural convection within an eccentric horizontal cylindrical annulus", *International Journal of Numerical Methods for Heat and Fluid Flow*, Vol. 26 No. 5, pp. 1346-1364.
- Hamza, N.H., Theeb, M.A. and Sheremet, M.A. (2023), "Heat transfer enhancement in a corrugated chamber filled with hybrid nanofluid under an influence of internal heated plate", *International Journal of Numerical Methods for Heat and Fluid Flow*, Vol. 33 No. 9, pp. 3094-3110.
- Huminic, G. and Huminic, A. (2020), "Entropy generation of nanofluid and hybrid nanofluid flow in thermal systems: a review", *Journal of Molecular Liquids*, Vol. 302, p. 112533.
- Huppert, H.E. and Sparks, R.S., J. (1984), "Double-diffusive convection due to crystallization in magmas", *Annual Review of Earth and Planetary Sciences*, Vol. 12 No. 1, pp. 11-37.
- Hussain, S., Öztop, H.F., Qureshi, M.A. and Abu-Hamdeh, N. (2020), "Double diffusive buoyancy induced convection in stepwise open porous cavities filled nanofluid", *International Communications in Heat and Mass Transfer*, Vol. 119, p. 104949.
- Kahveci, K. (2010), "Buoyancy driven heat transfer of nanofluids in a tilted enclosure", *ASME J. Heat Transfer*, Vol. 132, p. 62501.
- Kefayati, G.R. (2015), "FDLBM simulation of entropy generation in double diffusive natural convection of power-law fluids in an enclosure with Soret and Dufour effects", *International Journal of Heat and Mass Transfer*, Vol. 89, pp. 267-290.
- Kefayati, G.H.R. (2016a), "Simulation of double diffusive MHD (magnetohydrodynamic) natural convection and entropy generation in an open cavity filled with power-law fluids in the presence of Soret and Dufour effects (part I: study of fluid flow, heat and mass transfer)", *Energy*, Vol. 107, pp. 889-916.

- Kefayati, G.R. (2016b), "Simulation of double diffusive natural convection and entropy generation of power-law fluids in an inclined porous cavity with sores and dufour effects (part II: Entropy generation)", *International Journal of Heat and Mass Transfer*, Vol. 94, pp. 582-624.
- Kefayati, G.R. (2016c), "Simulation of double diffusive natural convection and entropy generation of power-law fluids in an inclined porous cavity with Soret and Dufour effects (part II: Entropy generation)", *International Journal of Heat and Mass Transfer*, Vol. 94, pp. 582-624.
- Kim, G.B., Hyun, J.M. and Kwak, H.S. (2003), "Transient buoyant convection of a power-law non-Newtonian fluid in an enclosure", *International Journal of Heat and Mass Transfer*, Vol. 46, pp. 3605-3617.
- Lamsaadi, M., Naimi, M., Hasnaoui, M. and Mamou, M. (2006), "Natural convection in a vertical rectangular cavity filled with a non-Newtonian power law fluid and subjected to a horizontal temperature gradient", *Numerical Heat Transfer, Part A: Applications*, Vol. 49 No. 10, pp. 969-990.
- M. Aly, A. (2020), "Incompressible smoothed particle hydrodynamics for MHD double-diffusive natural convection of a nanofluid in a cavity containing an oscillating pipe", *International Journal of Numerical Methods for Heat and Fluid Flow*, Vol. 30 No. 2, pp. 882-917.
- Mahian, O., Kolsi, L., Amani, M., Estellé, P., Ahmadi, G., Kleinstreuer, C., Marshall, J.S., Siavashi, M., Taylor, R.A., Niazmand, H. and Wongwises, S. (2019), "Recent advances in modeling and simulation of nanofluid flows-Part I: Fundamentals and theory", *Physics Reports*, Vol. 790, pp. 1-48.
- Mahmoodi, M. and Hashemi, S.M. (2012), "Numerical study of natural convection of a nanofluid in C-shaped enclosures", *International Journal of Thermal Sciences*, Vol. 55, pp. 76-89.
- Menbari, A., Alemrajabi, A.A. and Rezaei, A. (2016), "Heat transfer analysis and the effect of CuO/water nanofluid on direct absorption concentrating solar collector", *Applied Thermal Engineering*, Vol. 104, pp. 176-183.
- Okonkwo, E.C., Wole-Osho, I., Kavaz, D., Abid, M. and Al-Ansari, T. (2020), "Thermodynamic evaluation and optimization of a flat plate collector operating with alumina and iron Mono and hybrid nanofluids", *Sustainable Energy Technologies and Assessments*, Vol. 37, p. 100636.
- Raisi, A. (2016), "Natural convection of non-newtonian fluids in a square cavity with a localized heat source", *Strojniški vestnik - Journal of Mechanical Engineering*, Vol. 62 No. 10, pp. 553-564.
- Raizah, Z.A.S. and M. Aly, A. (2020), "ISPH method for MHD double-diffusive natural convection of a nanofluid within cavity containing open pipes", *International Journal of Numerical Methods for Heat and Fluid Flow*, Vol. 30 No. 7, pp. 3607-3634.
- Rashad, A.M., Elsayed Ahmed, S. and Ahmed Mansour, M. (2014), "Effects of chemical reaction and thermal radiation on unsteady double diffusive convection", *International Journal of Numerical Methods for Heat and Fluid Flow*, Vol. 24 No. 5, pp. 1124-1140.
- Reddy, P.S., Sreedevi, P. and Reddy, V.N. (2022a), "Entropy generation and heat transfer analysis of magnetic nanofluid flow inside a square cavity filled with carbon nanotubes", *Chemical Thermodynamics and Thermal Analysis*, Vol. 6, p. 100045.
- Reddy, P.S., Sreedevi, P. and Venkateswarlu, S. (2022b), "Impact of modified Fourier's heat flux on the heat transfer of MgO/Fe₃O₄-Eg-based hybrid nanofluid flow inside a square chamber", *Waves in Random and Complex Media*, doi: [10.1080/17455030.2022.2058112](https://doi.org/10.1080/17455030.2022.2058112).
- Roy, N.C. and Monira, S. (2023), "Natural convection of a reacting hybrid nanofluid in an open porous cavity bounded by vertical wavy walls", *International Journal of Numerical Methods for Heat and Fluid Flow*, Vol. 33 No. 9, pp. 3202-3227.
- Schmitt, R.W. (1994), "Double diffusion in oceanography", *Annual Review of Fluid Mechanics*, Vol. 26 No. 1, pp. 255-285.
- Seyyedi, S.M., Dogonchi, A.S., Hashemi-Tilehnoee, M., Ganji, D.D. and Chamkha, A.J. (2020), "Second law analysis of magneto-natural convection in a nanofluid filled wavy-hexagonal porous enclosure", *International Journal of Numerical Methods for Heat and Fluid Flow*, Vol. 30 No. 11, pp. 4811-4836.

-
- Shariatifard, A., Kamali, D., Hejri, S. and Hasani Malekshah, E. (2022), "Smoothed/profile lattice boltzmann method for hydrothermal analysis of a corrugated parabolic-trough solar collector filled with nanofluid predicted by koo-kleinstreuer-Li model", *International Journal of Numerical Methods for Heat and Fluid Flow*, Vol. 32 No. 5, pp. 1421-1439.
- Teamah, M.A. and El-Maghlany, W.M. (2010), "Numerical simulation of double-diffusive mixed convective flow in rectangular enclosure with insulated moving lid", *International Journal of Thermal Sciences*, Vol. 49 No. 9, pp. 1625-1638.
- Turner, J. (1974), "Double-diffusive phenomena", *Annual Review of Fluid Mechanics*, Vol. 6 No. 1, pp. 37-54.
- Usman, M., Khan, Z.H. and Liu, M.B. (2019), "MHD natural convection and thermal control inside a cavity with obstacles under the radiation effects", *Physica A: Statistical Mechanics and Its Applications*, Vol. 535, p. 122443.
- Verma, S.K., Tiwari, A.K. and Chauhan, D.S. (2017), "Experimental evaluation of flat plate solar collector using nanofluids", *Energy Conversion and Management*, Vol. 134, pp. 103-115.
- Yang, J.Q. and Zhao, B.X. (2021), "Numerical investigation of double-diffusive convection in rectangular cavities with different aspect ratio I: high-accuracy numerical method", *Computers and Mathematics with Applications*, Vol. 94, pp. 155-169.

Corresponding author

Manoj Kumar Nayak can be contacted at: mkn2122@gmail.com